ADVANCED FUNCTIONAL MATERIALS
www.afm-journal.de

Higher Order Topological Defects in a Moiré Lattice

*Eugenio Gambari, Sebastian Meyer, Sacha Guesne, Pascal David, François Debontridder, Laurent Limot, Fabrice Scheurer, Christophe Brun, Bertrand Dupé, Tristan Cren, and Marie Hervé**

Topological defects are ubiquitous, they manifest in a wide variety of systems such as liquid crystals, magnets or superconductors. The recent quest for non-abelian anyons in condensed matter physics stimulates the interest for topological defects since they can be hosted in vortices in quantum magnets or topological superconductors. In addition to these vortex defects, this study proposes to investigate edge dislocations in 2D magnets as new building blocks for topological physics since they can be described as vortices in the structural phase field. It demonstrates the existence of higher order topological dislocations within the higher order moiré pattern of the van der Waals 2D magnet $CrCl_3$ deposited on Au(111). Surprisingly, these higher order dislocations arise from ordinary simple edge dislocations in the atomic lattice of $CrCl_3$. This study provide a theoretical framework explaining the higher order dislocations as vortices with a winding Chern number of 2. It is expected that these original defects can stabilize some anyons either in a 2D quantum magnet or within a 2D superconductor coupled to it.

1. Introduction

Van der Waals materials are emerging as extremely versatile building blocks for many fields of research at the fundamental and applied level.[1,2] They offer tremendous possibilities for fine-tuning spintronics,[3,4] superconducting,[5–7] nanoelectronics,[1,2] and optical devices.[8,9] The toolbox of these heterostructures is continuously growing with for instance the recent discovery of ferromagnetic order in the family of chromium trihalides down to the monolayer limit, CrX_3 (X = I, Br, Cl).[10–14] Due to the absence of magnetic anisotropy in the plane when the $CrCl_3$ monolayer is decoupled from its substrate, it behaves as a 2D XY quantum magnet[14] that can host non-abelian anyons in the center of magnetic vortex cores.[15] Their integration in van der Waals heterostructures is expected to lead to a wealth of new exotic effects. Stacking chromium trihalides with transition metal dichalcogenides that exhibit a strong Ising spin-orbit coupling appears as a promising route towards the development of hybrid magnetic/superconducting systems.[5,6] For instance, topological superconductivity was recently discovered in $CrBr_3/NbSe_2$ heterostructures.[5,6] The proposed mechanisms leading to topological order in these structures were intimately related to the presence of a moiré pattern.[6] Several studies have related the observation of a moiré structure due to the mismatch between the CrX_3 monolayers and their substrate.[6,14,16,17] The orientational degree of freedom may add a supplementary possibility to tune the moiré, as observed in twisted CrX_3 bilayers.[18–20] The physics of moiré is quite complex, a same structure might exhibit several moiré patterns of different orders, as observed in Gr/Ir or Gr/Pt systems.[21–27] Higher order structures appear when, in a particular direction, n_1 lattice periods of layer 1 almost match with n_2 periods of layer 2. Correspondingly, in the reciprocal space, a higher order moiré appears when a small enough wave vector $\mathbf{q}_{moire} = m_1\mathbf{q}_1 - m_2\mathbf{q}_2$ can be defined with $\mathbf{q}_i$ being the Bragg vectors of the two lattices and $|\mathbf{q}_{moire}| \ll \mathrm{Min}(|\mathbf{q}_1|, |\mathbf{q}_2|)$. Interestingly, the CrX_3 compounds have a unit cell of almost twice the size the one of dense metals, this would naturally lead to a second order moiré where $m_1 = 1$ and $m_2 = 2$.

In the CrX_3 family, until now, magnetization was shown to be essentially collinear.[10,11,14,28,29] However, in CrI_3 bilayers, some hint of non-collinear magnetism was found. A sizeable spatial modulation of the magnetic exchange interaction[18,20,30–32] was ascribed to the moiré pattern. This confers an additional interest for the CrX_3 family. Indeed, a non-collinear magnetic order is predicted to be a major ingredient for inducing a topological

E. Gambari, S. Guesne, P. David, F. Debontridder, C. Brun, T. Cren, M. Hervé
Sorbonne Université
CNRS
Institut des Nanosciences de Paris
UMR7588, 4 place Jussieu, Paris 75005, France
E-mail: marie.herve@sorbonne-universite.fr

S. Meyer, B. Dupé
Université de Liège
Nanomat/Q-MAT
Sart Tilman B-4000, Belgium

S. Meyer, B. Dupé
Université de Liège
TOM/Q-MAT
Sart Tilman B-4000, Belgium

S. Meyer, B. Dupé
Fonds de la Recherche Scientifique (FRS-FNRS)
Bruxelles B-1000, Belgium

L. Limot, F. Scheurer
Université de Strasbourg
CNRS
Institut de Phsyique et Chime des Matériaux de Strasbourg
UMR7504, Strasbourg F-67000, France

The ORCID identification number(s) for the author(s) of this article can be found under https://doi.org/10.1002/adfm.202407438

DOI: 10.1002/adfm.202407438

order in superconducting/magnetic heterostructures.[33–37] Topological superconductors may host Majorana bound states localized on topological defects such as superconducting vortex cores or spin-orbit vortices,[38] but other kind of defects such as dislocations could also be of interest since edge dislocations are topological defects analogous to vortices.[39,40] Interestingly, a moiré pattern in van der Waals materials appears to be a promising candidate for investigating such physics. For instance, in graphene/Ir(111), graphene bilayers, and h-BN/Ru,[41–44] simple edge dislocations in the atomic lattice result in dislocations in the moiré pattern.

Here we report that $CrCl_3$/Au(111) produces large 2D islands that exhibit moiré patterns. In this case, since the $CrCl_3$ lattice period is very close to twice the one of Au(111), the moiré pattern is of order 2. It has been already observed that an atomic scale edge dislocation induces an edge dislocation in the resulting moiré lattice.[42–45] Here we show, experimentally and theoretically, that in a higher order moiré a simple edge dislocation induces a dislocation with a higher topological charge (Chern number); we also demonstrate that the charges of both dislocations can have opposite sign. The experiments reveal that the presence of a simple edge dislocation of topological charge 1 in the $CrCl_3$ lattice leads to a dislocation of topological charge −2. These observations are explained within a unified model. We show that a higher order moiré pattern is a way to access topological defects of higher Chern winding number. This unified model can be used as a predictive tool to build van der Waals heterostructures in order to engineer topological defects of the desired Chern winding numbers.

2. Results

2.1. Superstructures in $CrCl_3$ Monolayer on Au(111)

Crystalline chromium trichloride ($CrCl_3$) thin films were grown using molecular beam epitaxy (MBE) on a clean Au(111) substrate. **Figure 1a** depicts a large scale scanning tunneling microscopy (STM) topography of 1 ML thick islands of $CrCl_3$ on the bare Au(111) atomic terraces. The islands can show several in-plane crystalline orientations (see Note S1, Supporting Information). Throughout the manuscript, we will focus on the islands where the dense atomic directions of $CrCl_3$ align along the dense atomic directions of the Au substrate $< 1\bar{1}0 >_{Au}$. Our STM study shows that $CrCl_3$ is restoring the lattice parameter of a freestanding $CrCl_3$ monolayer (see Note S1, Supporting Information). Remarkably, upon cooling down the sample to 4K, a superstructure emerges within these $CrCl_3^{\alpha}$ islands, which is not visible at room temperature (see Figure S2, Supporting Information). Figure 1b shows an STM image featuring two islands labeled A and B, which form a twinned boundary (see Figure S4, Supporting Information). Both islands exhibit an hexagonal superstructure with a periodicity of 6.2 nm. Their orientation differs by an angle of 13° (see green and dark dashed lines). Interestingly, the rotation of the superstructure does not seem to be correlated with a rotation of the atomic lattice. Figure 1c presents the Fourier filtering of the STM topography of Figure 1b revealing the atomic structure of $CrCl_3$. The white dashed line serves as a visual guide, highlighting the dense atomic direction of $CrCl_3$ in both islands. At first sight, no misalignment of the crystal axis is detectable between these two islands. Additionally, within individual islands, the superstructure exhibits a distortion, while the atomic lattice seems to remain unaffected (Figure 1d,e). Figure 1d displays a STM topography acquired inside an island. The pink dashed line is a guide for the eyes showing that the superstructure is slightly undulated. Figure 1e shows the corresponding Fourier filtered image, revealing the atomic lattice of $CrCl_3$. The white dashed line that follows the dense atomic direction seems to be insensitive to the change of orientation in the superstructure. Nevertheless, we conducted modelisation of a moiré pattern in this system (see Note S5, Supporting Information) and showed that this superstructure is indeed a moiré effect exhibiting an unusual high sensitivity to subtle variations in the atomic lattice orientation. The change of orientation of the moiré pattern shown in Figure 1b,d is explained by a deviation angle in the atomic lattice of less than 1°. This system is rather rich, with plenty of different moiré patterns induced by very small deviations of the $CrCl_3$ lattice orientation with respect to Au(111). The system could be a good platform to explore the influence of a moiré on magnetic textures.

2.2. Role of Au(111) on the Electronic Structure

Our measurements show that $CrCl_3$ restores its lattice constant as in a freestanding monolayer (see Note S1.1, Supporting Information). In order to clarify the role of Au(111) on the electronic structure, we have performed tunneling spectroscopy experiments and density functional theory (DFT) calculations. **Figure 2a** shows scanning tunneling spectroscopy data for different positions on the moiré pattern of $CrCl_3$/Au(111). The differential conductance depends on the position on the moiré pattern, the resulting contrast in the image is therefore of spectroscopic origin (see Notes S3 and S6, Supporting Information). Regardless of the position, the conductance shows the same features: no intensity below 0.2 eV; then a small increase at 0.2 eV followed by a plateau and then a strong increase above 0.3 eV, eventually followed by a plateau at 1.2 eV. These spectroscopic features are qualitatively in agreement with our vacuum density of states (VacDOS) in Figure 2b following the Tersoff & Hamann model.[46–48] For an $CrCl_3$ unsupported monolayer (UML, cf. shaded area), we would expect peaks to occur at the Fermi energy and more significantly below the Fermi energy, where the experimental data do not show any states. A gap appears in between 0.2 and 1.4 eV, which is absent in the measurement of Figure 2a. Adding Au(111) underneath $CrCl_3$, the VacDOS changes drastically, shifting the bandgap to the Fermi level and below (black curve of panel b). Note that due to the computational effort of the DFT calculations, we adopt a perfect registry between $CrCl_3$ and Au(111) (for further details, see Experimental Section and Note S7, Supporting Information). Nevertheless, the calculated VacDOS exhibits qualitatively the same trends of the measurement: the bandgap and the shoulder/peak structures at 0.2 and 1.7 eV. We attribute the differences between the calculations and the measurements to the differing structures within the calculations. From this comparison, we deduce that Au(111) has an influence on the electronic structure of $CrCl_3$ and that this system is not solely driven

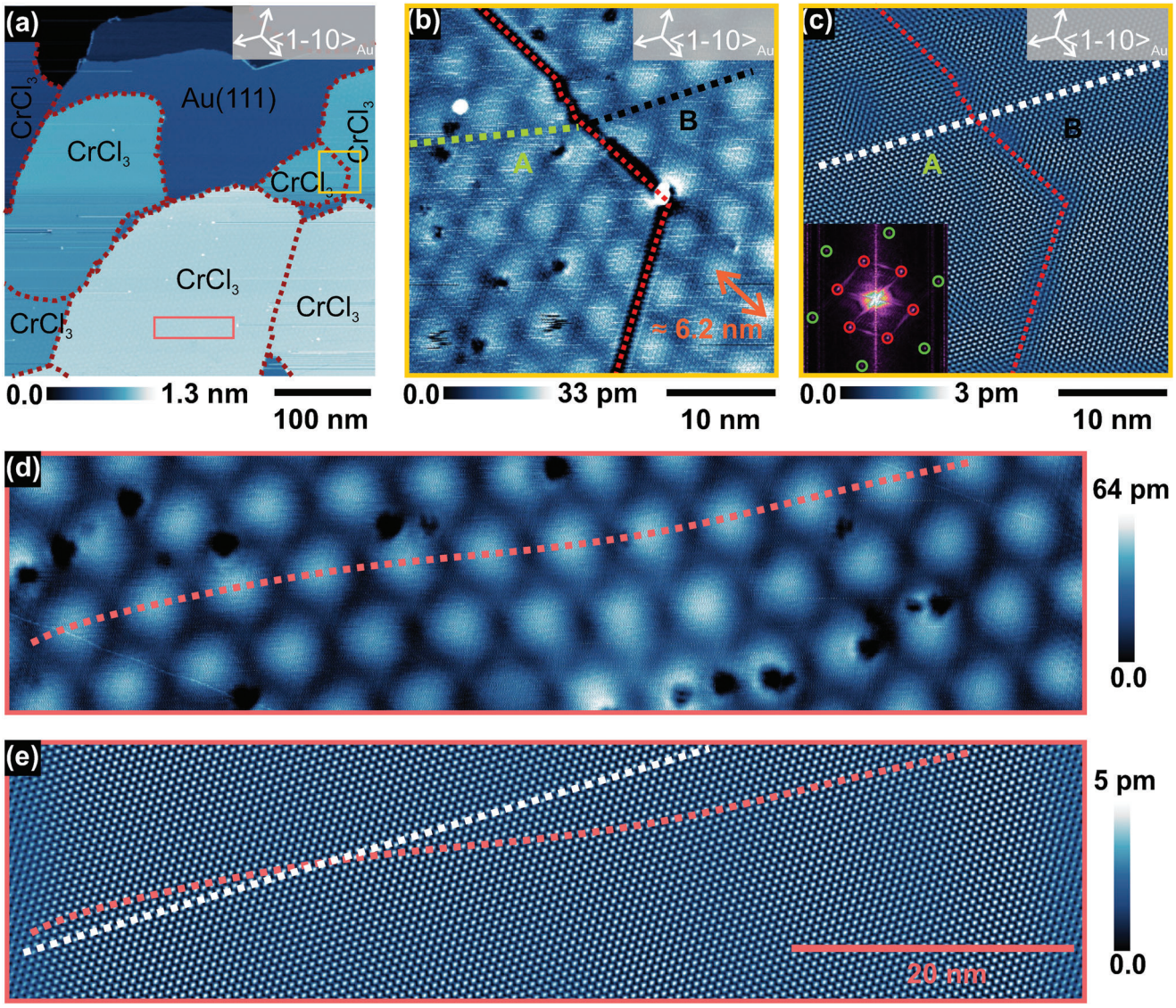

Figure 1. Superstructure in $CrCl_3$/Au(111). a) Large scale STM topography of 0.6 monolayers of $CrCl_3$ deposited on a Au(111) substrate. The red dashed line marks out the $CrCl_3$ islands. b) Zoom in the yellow frame of (a) showing 2 structural domains where the superstructure orientation differs by an angle of 13°. The green and dark dashed lines are guides for the eyes to follow the orientation of the superstructure in the two domains, the red dashed line shows the separation between the two islands. c) Fourier filtered image revealing the atomic lattice of $CrCl_3$ in the two structural domains. The white dashed line is a guide for the eyes to follow the orientation of the atomic lattice. The Fourier filtering is obtained by selecting the Bragg spots marked in red and green in the reciprocal space image shown in the inset. d) STM topography acquired in the pink frame of (a) showing that the superstructure is wavy inside a $CrCl_3$ island, while no rotation of the atomic lattice can be detected in the Fourier filtered image e). The pink and white dashed lines are eye-guides to follow the orientation of the superstructure and the atomic lattice inside the island. For all the STM images, the tunneling parameters are: Bias voltage $U_0 = 2V$; Tunneling current $I_t = 200pA$.

by van der Waals forces. This is in accordance with reference [49], where the authors compared the binding energies and concluded that for $CrCl_3$/Au(111) these energies lie at the threshold of van der Waals and ionic bonds.

2.3. Higher Order Edge Dislocations of the Moiré Pattern

Very peculiar defects have been observed in this moiré pattern. They consist in higher order edge dislocations. One such defect is illustrated in **Figure** 3a. On the left side of the dislocation, marked by green arrows, three rows of the moiré pattern merge into a single row on the right side, resulting in the disappearance of a pair of rows. Notably, similar dislocations have been observed at various points in the sample. In every case, a pair of rows disappears, highlighting a distinctive feature of this particular moiré pattern.

To further characterize the dislocation, we analyze its Burgers vector (Figure 3b) and coordination (Figure 3c). The Burgers vector of the dislocation is found to be twice the lattice vector of the moiré pattern: $\boldsymbol{b}_{moiré} = -2\boldsymbol{a}^1_{moiré}$. The coordination of the

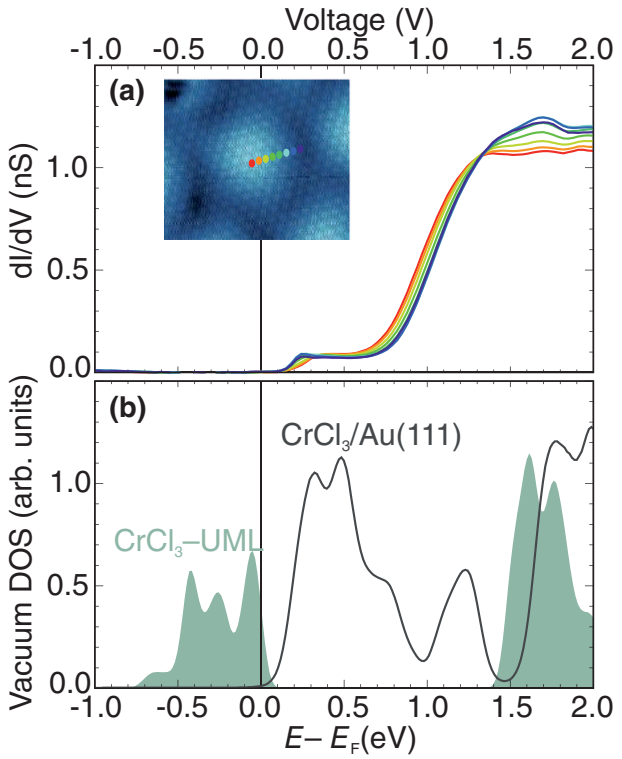

Figure 2. Role of Au(111) on the electronic structure. Comparison between experimentally measured spectroscopy data and calculated vacuum density of states of $CrCl_3$/Au(111). a) Scanning tunneling spectroscopy measurements on different positions of the moiré pattern as indicated in the inset. Setpoint: U_0 = 2V, I_t = 400pA, these data were recorded using lock-in with a modulation of 20 mV rms added to the bias voltage. b) Density functional theory calculations of the vacuum density of states 3 Å above the surface of a $CrCl_3$ unsupported monolayer UML (green area) in comparison with $CrCl_3$/Au(111) (black line). Note that in the calculations $CrCl_3$ is assumed to be in perfect registry with Au(111), meaning that the moiré is not taken into account.

lattice cells surrounding the dislocation is determined to be 5-5-8, i.e. two cells are five-fold coordinated while one is eight-fold, this is in contrast with ordinary 5–7 dislocations. To gain insight into the atomic structure surrounding the dislocation, Figure 3d displays a magnified view around the dislocation. Remarkably, at the exact position of the dislocation in the moiré pattern, we observe an edge dislocation in the atomic lattice of $CrCl_3$. Specifically, one row of atoms on the left side of the dislocation transforms into two rows on the right side. Prior studies in the literature have suggested that a dislocation or defect within a moiré pattern faithfully replicates the corresponding dislocation or defect at the atomic level.[42–45] In this case, the dislocation at the atomic level is characterized by a 5–7 defect and a Burgers vector $\boldsymbol{b}_{CrCl_3} = \boldsymbol{a}^1_{CrCl_3}$ (see red arrow in Figure 3d) which differs with the Burgers vector of the dislocation in the moiré pattern.

To understand the particularity of this dislocation in the moiré pattern, we model our system by introducing a 5–7 defect in the atomic lattice of $CrCl_3$ and convolute it with a defect-free atomic lattice of Au(111). Figure 3e illustrates the result of this simulation, which successfully reproduces the experimental observations of a dislocation with a Burgers vector $\boldsymbol{b}_{moiré} = -2\boldsymbol{a}^1_{moiré}$.

2.4. Analytical Description

To comprehend the physical origin of the observed moiré pattern and its peculiar dislocations, we performed an analytical analysis of the moiré pattern. A conventional approach to describe a moiré pattern employs a continuous model.[21] The moiré pattern can be described as the result of the interaction between two lattice functions, $f_1(x, y)$ and $f_2(x, y)$ representing the superposition of plane waves, on a constant background with corresponding spatial frequencies Q_1 and Q_2. To explain this in the simplest terms, we consider the case where the waves in each lattice propagate along the x-direction. The product between two lattice functions $f_1(x, y) \times f_2(x, y) = (1 + a\cos(Q_1 x)) \times (1 + a\cos(Q_2 x))$, with a an arbitrary constant, can be rewritten as:

$$f_1 \times f_2 = 1 + \frac{a^2}{2}\left(\cos[(Q_1 + Q_2)x] + \cos[(Q_1 - Q_2)x]\right) + \\ +2a\cos\left[\frac{(Q_1+Q_2)}{2}x\right]\cos\left[\frac{(Q_1-Q_2)}{2}x\right] \quad (1)$$

We obtain the addition of 3 terms: a constant background and 2 periodic functions. In the following, we will consider only the first periodic function to describe the moiré. It is a sum of two cosines, with one slowly varying term $\cos[(Q_1 - Q_2)x]$ that stems for the moiré term. The resulting spatial beating frequency, $Q_1 - Q_2$ corresponds to the spatial frequency of the moiré, Q_{moire}. For the case of a moiré formed between two hexagonal lattices as for $CrCl_3$/Au(111), each lattice must be treated as the superposition of two waves traveling in directions separated by an angle of 120°. This makes the mathematical description in real space quite complex. A simpler way to describe a moiré is to treat the problem in the reciprocal space, where the moiré wave vector is the difference between the wave vectors of each atomic lattice. We employed the intelligible model described by Zeller et al. and Le Ster et al.[21,50] Within this framework, not only the 1st order, but also the higher order Fourier component of the moiré need to be considered.

The general reciprocal vectors for both atomic lattices, $\boldsymbol{Q}^{i,j}_{Au}$ and $\boldsymbol{Q}^{k,l}_{CrCl_3}$ are expressed as linear combinations of the primitive reciprocal lattice vectors $\boldsymbol{Q}^{1,0}_{Au}$, $\boldsymbol{Q}^{0,1}_{Au}$, $\boldsymbol{Q}^{1,0}_{CrCl_3}$, $\boldsymbol{Q}^{0,1}_{CrCl_3}$:

$$\boldsymbol{Q}^{i,j}_{Au} = i\boldsymbol{Q}^{1,0}_{Au} + j\boldsymbol{Q}^{0,1}_{Au} \quad (2)$$

$$\boldsymbol{Q}^{k,l}_{CrCl_3} = k\boldsymbol{Q}^{1,0}_{CrCl_3} + l\boldsymbol{Q}^{0,1}_{CrCl_3} \quad (3)$$

Here $|\boldsymbol{Q}^{1,0}_{Au}| = |\boldsymbol{Q}^{0,1}_{Au}| = 2\pi/a_{Au}$ and $|\boldsymbol{Q}^{1,0}_{CrCl_3}| = |\boldsymbol{Q}^{0,1}_{CrCl_3}| = 2\pi/a_{CrCl_3}$, where a_{Au} = 0.288nm and a_{CrCl_3} = 0.604 nm correspond to the lattice parameters of Au and $CrCl_3$, respectively. The possible Fourier components of the moiré pattern's reciprocal vectors are expressed as the difference between the corresponding reciprocal vectors of Au and $CrCl_3$:

$$\boldsymbol{Q}^{i,j,k,l}_{moiré} = \boldsymbol{Q}^{i,j}_{Au} - \boldsymbol{Q}^{k,l}_{CrCl_3} \quad (4)$$

When the dense atomic directions of $CrCl_3$ align with the $\langle 1\bar{1}0\rangle_{Au}$ directions, $\boldsymbol{Q}^{1,0}_{Au}$ is collinear with $\boldsymbol{Q}^{1,0}_{CrCl_3}$ (**Figure 4a**). Let us illustrate why one should here consider higher order moiré by first showing that a usual first order moiré doesn't correspond to

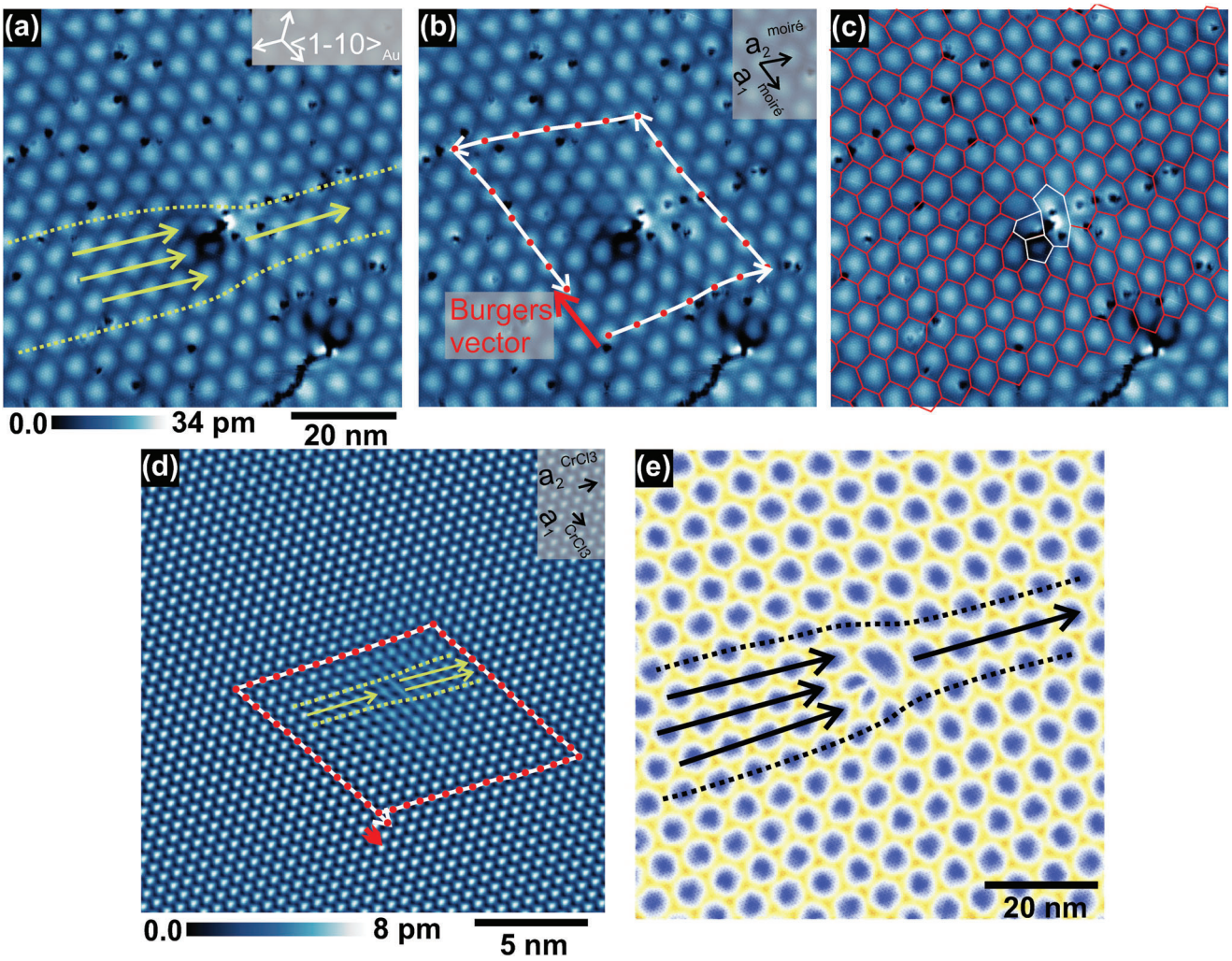

Figure 3. Higher order edge dislocations. a) STM topograhy showing a double dislocation in the moiré pattern. The dashed green lines and arrows are guides for the eyes to follow the dislocation. (U_0 = 2V, I_t = 200pA). b) Drawing of the Burgers circuit around the dislocation. c) Coordination of the dislocation in the moiré. d) Zoom around the dislocation in the moiré pattern, the STM topography was Fourier filtered to reveal the atomic lattice. It shows a simple dislocation in the atomic lattice of $CrCl_3$ at the exact position of the dislocation in the moiré pattern. e) Numerical simulation of the dislocation in the moiré pattern.

our observations. The first order moiré wave vector formed between the (1,0) Bragg spots of Au and $CrCl_3$ is:

$$Q_{moiré}^{1,0,1,0} = Q_{Au}^{1,0} - Q_{CrCl_3}^{1,0} \tag{5}$$

This results in a moiré period in real space:

$$L_{moiré}^{1,0,1,0} = 2\pi/|Q_{moiré}^{1,0,1,0}| = 0.55\,\text{nm} \tag{6}$$

This period is notably smaller than a_{CrCl_3} (0.604 nm). A moiré pattern between the (1,0) Bragg spots of Au and $CrCl_3$ is meaningless. This emanates from the fact that a_{CrCl_3} exceeds the lattice parameter of Au by more than a factor two. $CrCl_3$/Au(111) is a model case where higher order moiré is popping up. Extending the reciprocal lattice of $CrCl_3$ to the second order (Figure 4b) reveals that the shortest moiré wave vector is formed between the (1,0) Bragg spot of Au and the (2,0) Bragg spot of $CrCl_3$, expressed as:

$$Q_{moiré}^{1,0,2,0} = Q_{Au}^{1,0} - Q_{CrCl_3}^{2,0} \tag{7}$$

In the real space, this yields a moiré pattern period:

$$L_{moiré}^{1,0,2,0} = 2\pi/|Q_{moiré}^{1,0,2,0}| = 6.2\,\text{nm} \tag{8}$$

which corresponds exactly to the period we measure in our experiments.

We will now explain the emergence of the peculiar dislocations (Figure 3). As a dislocation is a punctual defect that cannot be modeled easily in reciprocal space, the problem needs to be partially treated in real space. In order to avoid a heavy mathematical description and maintain conceptual clarity, we will consider a dislocation in a simple planar wave that can be modeled by a

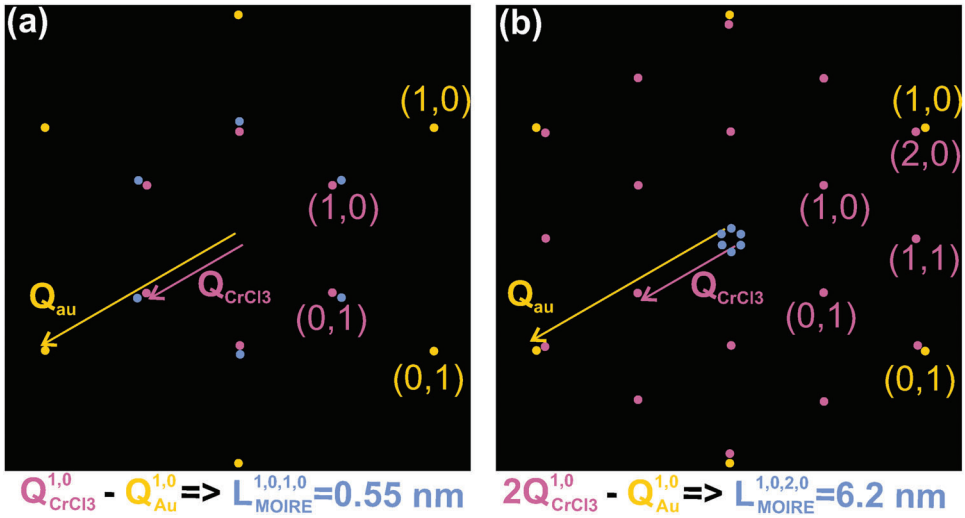

Figure 4. Reciprocal lattice of $CrCl_3$/Au(111). The blue dots correspond to the 1st a) and 2nd b) order moiré spots.

$\cos[(Q_1 x + \Delta\varphi(x, y)]$, with $\Delta\varphi(x, y)$ being a Berry phase associated to the defect. If one considers a dislocation located at the origin, $\Delta\varphi(x, y)$ can just be taken as the angle of the position vector $\boldsymbol{r} = (x, y)$ to the abscissa, i.e. $\Delta\varphi(x, y) = \arg(x + iy)$. The resulting dislocation pattern is shown in **Figure** 5a.

Consider now two lattices forming a first order moiré, with a dislocation in one of the lattices. It naturally results in a dislocation in the moiré pattern (Figure 5b). This can easily be explained using Equation 1. The moiré term is $\cos[((Q_1 - Q_2)x + \Delta\varphi(x, y)]$ which also exhibits a Berry phase that gives a dislocation in

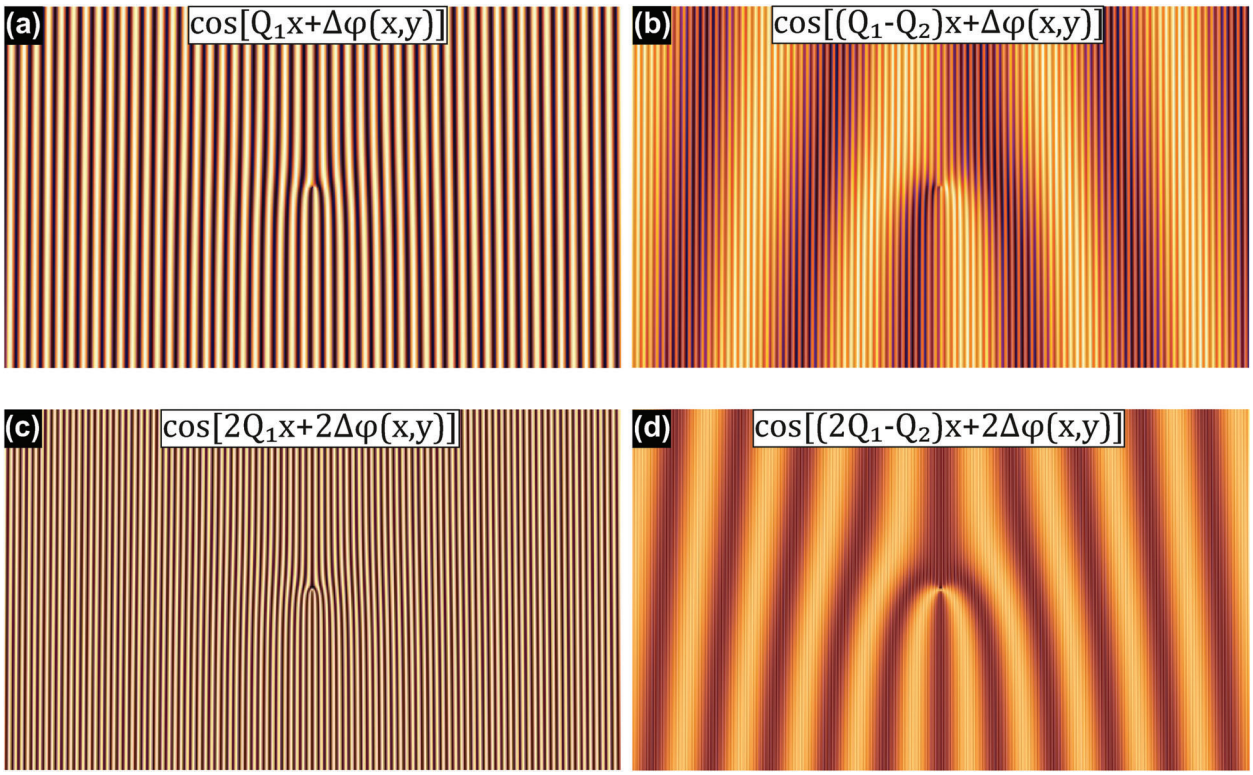

Figure 5. Analytical description of the dislocation in the moiré pattern. a) First order periodic lattice simulated by a simple plane wave in which a dislocation has been introduced in the form of phase difference corresponding to a Berry phase: $\Delta\varphi(x, y)$. b) First order moiré pattern when a simple dislocation exists in one of the two periodic lattices: a simple dislocation appears in the moiré. The dislocation in the moiré pattern exhibits the same Berry phase as in the primary lattice. c) Second order primary lattice: the Berry phase of the dislocation is doubled ($2\Delta\varphi(x, y)$) with respect to the first order shown in (a). d) The resulting second order moiré pattern shows an additional double row with a Berry phase ($2\Delta\varphi(x, y)$).

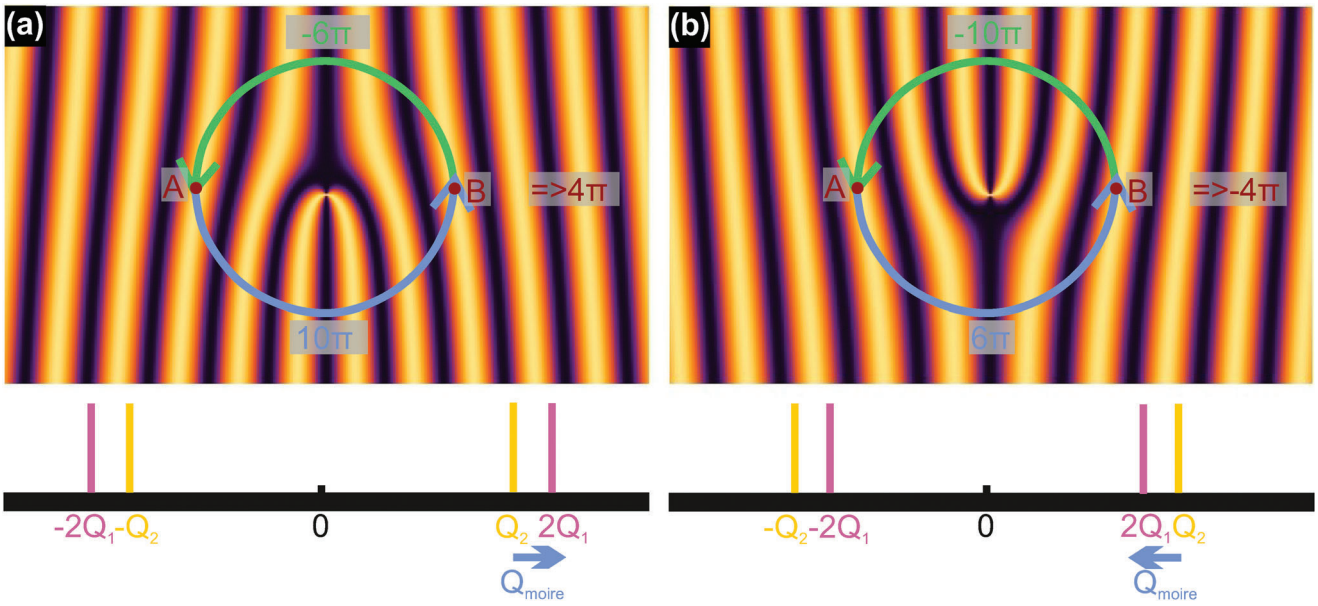

Figure 6. Dislocation's Berry phase. Dislocation in the 2nd order moiré when $2Q_1 > Q_2$ a) and $2Q_1 < Q_2$ b).

the moiré pattern. The question that immediately arises is what about our higher order moiré? The second order moiré is a beating between $\cos(2Q_1x)$ and $\cos(Q_2x)$, however, in the presence of a dislocation the phase Q_1x has to be replaced by $(Q_1x + \Delta\varphi(x, y))$. This results in a beating between $\cos[2(Q_1x + \Delta\varphi(x, y))]$ and $\cos(Q_2x)$ that leads to a moiré term $\cos[(2Q_1 - Q_2)x + 2\Delta\varphi(x, y)]$. As we can see, the resulting Berry phase is now $2\Delta\varphi(x, y)$, the double of the Berry phase in the primary defect. Figure 5c,d shows the resulting dislocation patterns in the second order lattice and its moiré pattern.

In Figure 5 one can see that the additional rows in the moiré and in the primary lattice are on the same side (bottom part of the images). This is at odds with what we observe in our experiments (Figure 3a,d). There, the additional rows in the atomic and moiré lattices are located at the opposite sides of the dislocation. This peculiarity is explained in **Figure 6**. Let us first assume that the additional row in the primary lattice is located at the bottom of the image (Figure 5a,c). To first order, it corresponds to a term $\cos(Q_1x + \Delta\varphi(x, y))$. Then, the second order moiré pattern is given by the expression $\cos((2Q_1 - Q_2)x + 2\Delta\varphi(x, y))$. In Figure 6 we show that depending on the sign of $(2Q_1 - Q_2)$, the dislocation in the moiré pattern can appear either on the same side of the dislocation in the primary lattice ($2Q_1 - Q_2 > 0$, Figure 6a), or in the opposite side ($2Q_1 - Q_2 < 0$, Figure 6b). To demonstrate this, let us consider the phase term $(2Q_1 - Q_2)x + 2\Delta\varphi(x, y)$ over a circuit surrounding the dislocation (see Figure 6a,b). In the case where $2Q_1 > Q_2$ (Figure 6a), along the blue arc, from A to B, the optical path difference $\Delta\theta$ is the sum of two positive contributions $\Delta\theta_1 = (2Q_1 - Q_2)\Delta x + 2\pi$, while for the green arc, from B to A, the optical path difference is the sum of a negative term and a positive one $\Delta\theta_2 = -(2Q_1 - Q_2)\Delta x + 2\pi$. Hence, $|\Delta\theta_1| - |\Delta\theta_2| = 4\pi$, which means that the blue arc encompasses two additional fringes compared to the green arc. Now, in the case where $2Q_1 < Q_2$ (Figure 6b), the situation is reversed. On the blue circuit the two phase shifts are opposite while on the green arc they add, this leads to the appearance of two additional rows in the top part of Figure 6b, while in the primary lattice the dislocation is still located at the bottom (Figure 5). The situation depicted in Figure 6b is in perfect agreement with our experimental observations (Figure 3a,d) and is consistent with the fact that $2Q_{CrCl3} < Q_{Au}$. The double dislocation in $CrCl_3$/Au(111) is carrying a Berry phase of -4π, corresponding to a Chern winding number of -2, which is equivalent to a double vortex.

3. Conclusion and Outlook

We have observed a higher order moiré pattern in a monolayer of $CrCl_3$ on a Au(111) surface that is driven by a large lattice mismatch: two periods of Au(111) matching almost one period of $CrCl_3$. The moiré originates mainly from an electronic structure modulation due to a strong coupling to the substrate. This interaction with the substrate was ascertained by DFT calculations that reveal a substantial shift of the chemical potential in $CrCl_3$ as compared to a free standing monolayer. The in situ grown samples exhibit single edge dislocations in the $CrCl_3$ monolayer that manifest as double dislocations in the moiré pattern. This doubling effect is a direct consequence of the second order moiré. The dislocations in the moiré pattern are structural topological defects which can be described, in the continuous limit, as double vortices carrying Berry phases of 4π. Our model can be used with many different systems and may serve to identify interesting ones that might host topological defects with a well controlled Chern number.

Due to the substantial coupling to a substrate with a Rashba spin-orbit coupling, $CrCl_3$/Au(111) could be an interesting platform for the stabilization of exotic non-collinear magnetic textures induced by the periodic potential of the moiré. The dislocations/vortices observed in the moiré pattern could be potentially interesting to pin topological spin textures that may host non conventional excitations such as non-abelian anyons. It

Table 1. Lattice parameters in Å used for vacuum LDOS in Figure 2b. $a_{\text{in-plane}}$ denotes the in-plane lattice constant of the hexagonal lattice, $\Delta d_{\text{Cl-Cr}}$ is the vertical distance between the Cl layers and the Cr layer, $\Delta d_{\text{CrCl}_3-\text{Au(111)}}$ denotes the vertical distance between $CrCl_3$ and the Au(111) surface.

System	$a_{\text{in-plane}}$ (Å)	$\Delta d_{\text{Cl-Cr}}$ (Å)	$\Delta d_{\text{CrCl}_3-\text{Au(111)}}$ (Å)
$CrCl_3$ UML	5.909	1.289	–
$CrCl_3$/Au(111)	5.909	1.336	4.233

has been recently proposed in $CrBr_3/NbSe_2$, that the moiré was responsible of the appearance of topological superconductivity in $NbSe_2$.[6] We may expect that topological defects in the moiré pattern of $CrBr_3$ could stabilize Majorana bound states.

4. Experimental Section

The experiments were performed under ultra high vacuum. The Au(111) single crystal was cleaned by cycles of argon-ion sputtering and annealing to 450 °C. Anhydrous powder of $CrCl_3$ was carefully degassed before being evaporated using a Knudsen cell on the clean Au(111) substrate at room temperature. To obtain flat $CrCl_3$ islands, the sample was post annealed to ≈150 °C for few minutes. STM experiments were performed at 4K in a home built low temperature STM and on a LT omicron commercial STM.

Density Functional Theory Calculations: The vacuum density of states calculations in Figure 2b have been done using the FLAPW method implemented in the code FLEUR.[51] Shown are two VacDOS calculations of a $CrCl_3$ UML and the $CrCl_3$ monolayer on top of a Au(111) surface. The presented VacDOS was calculated ≈3 Å above the surface. Since the unit cell of the moiré pattern with its substrate was too large for being feasible in first principles calculations, the atomic positions of both Cr and Cl atoms were placed in a perfect hexagonal structure where, a lattice constant in between Au bulk and $CrCl_3$ had been applied. The lattice parameters and distances used are presented in **Table 1**. Tests (see Supporting Information) varying the lattices constants of Au and $CrCl_3$, distance of $CrCl_3$ to the Au(111) surface and position of $CrCl_3$ w.r.t. the Au(111) atoms had shown no significant differences in their respective VacDOS, meaning the peaks' widths, heights, and forms are slightly differing with all these structural differences but the main features persist: the bandgap below the Fermi energy and the states occurring above E_F. For this reason, the VacDOS was showed for a lattice constant chosen in between the value of Au bulk and the $CrCl_3$ triclinic structure. The Au(111) substrate was modeled with three layers of Au to account for the ABC stacking of the fcc(111) lattice. Here, tests revealed that simply the presence of one monolayer of Au was enough to shift the bandgap of the $CrCl_3$ UML below the Fermi energy. For the calculation, a plane wave cutoff of $k_{\max} = 4.3$ a.u^{-1} and 288 k points were used in the irreducible wedge of the Brillouin zone.

Supporting Information

Supporting Information is available from the Wiley Online Library or from the author.

Acknowledgements

The authors acknowledged Johann Coraux for his thoughtful reading of the paper. This work was supported by the French Agence Nationale de la Recherche through the contract ANR GINET2-0 (ANR-20-CE42-0011). E.G. acknowledged the GDR-NS-CPU for funding it research stay in IPCMS. Computing time was provided by the Consortium d'Équipements de Calcul Intensif (FRS-FNRS Belgium GA 2.5020.11) and the LUMI CECI/Belgium for awarding this project access to the LUMI supercomputer, owned by the EuroHPC Joint Undertaking, hosted by CSC (Finland) and the LUMI consortium through LUMI CECI/Belgium, ULiege-NANOMAT-SKYRM-1. S.M. is a Postdoctoral Researcher [CR] of the Fonds de la Recherche Scientifique – FNRS (F.R.S-.FNRS no. CR 1.B.324.24F). B.D. is a Research Associate [CQ] of the Fonds de la Recherche Scientifique (F.R.S.–FNRS).

Conflict of Interest

The authors declare no conflict of interest.

Data Availability Statement

The data that support the findings of this study are available from the corresponding author upon reasonable request.

Keywords

density functional theory, moiré pattern, scanning tunneling microscopy, scanning tunneling spectroscopy, topological defects, transition metal surfaces, van der waals materials

Received: April 30, 2024
Revised: June 25, 2024
Published online:

[1] A. K. Geim, I. V. Grigorieva, *Nature* **2013**, *499*, 419.
[2] K. S. Novoselov, A. Mishchenko, A. Carvalho, A. H. Castro Neto, *Science* **2016**, *353*, aac9439.
[3] Q. H. Wang, A. Bedoya-Pinto, M. Blei, A. H. Dismukes, A. Hamo, S. Jenkins, M. Koperski, Y. Liu, Q.-C. Sun, E. J. Telford, H. H. Kim, M. Augustin, U. Vool, J.-X. Yin, L. H. Li, A. Falin, C. R. Dean, F. Casanova, R. F. L. Evans, M. Chshiev, A. Mishchenko, C. Petrovic, R. He, L. Zhao, A. W. Tsen, B. D. Gerardot, M. Brotons-Gisbert, Z. Guguchia, X. Roy, S. Tongay, et al., *ACS Nano* **2022**, *16*, 6960.
[4] W. Han, R. K. Kawakami, M. Gmitra, J. Fabian, *Nat. Nanotechnol.* **2014**, *9*, 794.
[5] S. Kezilebieke, M. N. Huda, V. Vaňo, M. Aapro, S. C. Ganguli, O. J. Silveira, S. Głodzik, A. S. Foster, T. Ojanen, P. Liljeroth, *Nature* **2020**, *588*, 424.
[6] S. Kezilebieke, V. Vaňo, M. N. Huda, M. Aapro, S. C. Ganguli, P. Liljeroth, J. L. Lado, *Nano Lett.* **2022**, *22*, 328.
[7] J. Martinez-Castro, T. Wichmann, K. Jin, T. Samuely, Z. Lyu, J. Yan, O. Onufriienko, P. Szabó, F. S. Tautz, M. Ternes, F. Lüpke, ArXiv **2023**, :2304.08142.
[8] D. N. Basov, M. M. Fogler, F. J. García de Abajo, *Science* **2016**, *354*, aag1992.
[9] Q. Zhang, G. Hu, W. Ma, P. Li, A. Krasnok, R. Hillenbrand, A. Alú, C.-W. Qiu, *Nature* **2021**, *597*, 187.
[10] B. Huang, G. Clark, E. Navarro-Moratalla, D. R. Klein, R. Cheng, K. L. Seyler, D. Zhong, E. Schmidgall, M. A. McGuire, D. H. Cobden, W. Yao, D. Xiao, P. Jarillo-Herrero, X. Xu, *Nature* **2017**, *546*, 270.
[11] W. Chen, Z. Sun, Z. Wang, L. Gu, X. Xu, S. Wu, C. Gao, *Science* **2019**, *366*, 983.
[12] M. Kim, P. Kumaravadivel, J. Birkbeck, W. Kuang, S. G. Xu, D. G. Hopkinson, J. Knolle, P. A. McClarty, A. I. Berdyugin, M. Ben Shalom, R. V. Gorbachev, S. J. Haigh, S. Liu, J. H. Edgar, K. S. Novoselov, I. V. Grigorieva, A. K. Geim, *Nat. Electron.* **2019**, *2*, 457.
[13] D. Soriano, M. I. Katsnelson, J. Fernández-Rossier, *Nano Lett.* **2020**, *20*, 6225.

[14] A. Bedoya-Pinto, J.-R. Ji, A. K. Pandeya, P. Gargiani, M. Valvidares, P. Sessi, J. M. Taylor, F. Radu, K. Chang, S. S. P. Parkin, *Science* **2021**, *374*, 616.
[15] A. Kitaev, *Ann. Phys.* **2006**, *321*, 2.
[16] S. C. Ganguli, M. Aapro, S. Kezilebieke, M. Amini, J. L. Lado, P. Liljeroth, *Nano Lett.* **2023**, *23*, 3412.
[17] P. Li, C. Wang, J. Zhang, S. Chen, D. Guo, W. Ji, D. Zhong, *Sci. Bull.* **2020**, *65*, 1064.
[18] H. Xie, X. Luo, Z. Ye, Z. Sun, G. Ye, S. H. Sung, H. Ge, S. Yan, Y. Fu, S. Tian, H. Lei, K. Sun, R. Hovden, R. He, L. Zhao, *Nat. Phys.* **2023**, *19*, 1150.
[19] Z. Qiu, M. Holwill, T. Olsen, P. Lyu, J. Li, H. Fang, H. Yang, M. Kashchenko, K. S. Novoselov, J. Lu, *Nat. Commun.* **2021**, *12*, 70.
[20] G. Cheng, M. M. Rahman, A. L. Allcca, A. Rustagi, X. Liu, L. Liu, L. Fu, Y. Zhu, Z. Mao, K. Watanabe, T. Taniguchi, P. Upadhyaya, Y. P. Chen, *Nat. Electron.* **2023**, *6*, 434.
[21] P. Zeller, S. Günther, *New J. Phys.* **2014**, *16*, 083028.
[22] E. Loginova, S. Nie, K. Thürmer, N. C. Bartelt, K. F. McCarty, *Phys. Rev. B* **2009**, *80*, 085430.
[23] P. Zeller, S. Dänhardt, S. Gsell, M. Schreck, J. Wintterlin, *Surf. Sci.* **2012**, *606*, 1475.
[24] N. Blanc, J. Coraux, C. Vo-Van, A. T. N'Diaye, O. Geaymond, G. Renaud, *Phys. Rev. B* **2012**, *86*, 235439.
[25] A. T. N'Diaye, J. Coraux, T. N. Plasa, C. Busse, T. Michely, *New J. Phys.* **2008**, *10*, 043033.
[26] P. Merino, M. Švec, A. L. Pinardi, G. Otero, J. A. Martín-Gago, *ACS Nano* **2011**, *5*, 5627.
[27] A. Artaud, L. Magaud, T. Le Quang, V. Guisset, P. David, C. Chapelier, J. Coraux, *Sci. Rep.* **2016**, *6*, 25670.
[28] I. Tsubokawa, *J. Phys. Soc. Jpn.* **1960**, *15*, 1664.
[29] C. Starr, F. Bitter, A. R. Kaufmann, *Phys. Rev.* **1940**, *58*, 977.
[30] M. Akram, H. LaBollita, D. Dey, J. Kapeghian, O. Erten, A. S. Botana, *Nano Lett.* **2021**, *21*, 6633.
[31] D. Ghader, B. Jabakhanji, A. Stroppa, *Commun. Phys.* **2022**, *5*, 1.
[32] A. O. Fumega, J. L. Lado, *2D Mater.* **2023**, *10*, 025026.
[33] S. Nakosai, Y. Tanaka, N. Nagaosa, *Phys. Rev. B* **2013**, *88*, 180503.
[34] W. Chen, A. P. Schnyder, *Phys. Rev. B* **2015**, *92*, 214502.
[35] G. Yang, P. Stano, J. Klinovaja, D. Loss, *Phys. Rev. B* **2016**, *93*, 224505.
[36] N. Mohanta, T. Zhou, J.-W. Xu, J. E. Han, A. D. Kent, J. Shabani, I. Žutić, A. Matos-Abiague, *Phys. Rev. Appl.* **2019**, *12*, 034048.
[37] M. Garnier, A. Mesaros, P. Simon, *Commun. Phys.* **2019**, *2*, 1.
[38] G. C. Ménard, A. Mesaros, C. Brun, F. Debontridder, D. Roditchev, P. Simon, T. Cren, *Nat. Commun.* **2019**, *10*, 2587.
[39] J. F. Nye, M. V. Berry, *Proc. R. Soc. London, Ser. A* **1974**, *336*, 165.
[40] C. Dutreix, H. González-Herrero, I. Brihuega, M. I. Katsnelson, C. Chapelier, V. T. Renard, *Nature* **2019**, *574*, 219.
[41] J. Coraux, A. T. N'Diaye, C. Busse, T. Michely, *Nano Lett.* **2008**, *8*, 565.
[42] J. Lu, L. C. Gomes, R. W. Nunes, A. H. Castro Neto, K. P. Loh, *Nano Lett.* **2014**, *14*, 5133.
[43] P. Pochet, B. C. McGuigan, J. Coraux, H. T. Johnson, *Appl. Mater. Today* **2017**, *9*, 240.
[44] T. A. de Jong, T. Benschop, X. Chen, E. E. Krasovskii, M. J. A. de Dood, R. M. Tromp, M. P. Allan, S. J. van der Molen, *Nat. Commun.* **2022**, *13*, 70.
[45] H. Yang, T. Zhang, M. Liu, L. Liu, X. Wu, Y. Wang, *ACS Appl. Electron. Mater.* **2022**, *4*, 891.
[46] J. Bardeen, *Phys. Rev. Lett.* **1961**, *6*, 57.
[47] J. Tersoff, D. R. Hamann, *Phys. Rev. B* **1985**, *31*, 805.
[48] D. Wortmann, S. Heinze, P. Kurz, G. Bihlmayer, S. Blügel, *Phys. Rev. Lett.* **2001**, *86*, 4132.
[49] F. Zhang, X. Li, Y. Wu, X. Wang, J. Zhao, W. Gao, *Phys. Rev. B* **2022**, *106*, L100407.
[50] M. L. Ster, T. Märkl, S. A. Brown, *2D Mater.* **2019**, *7*, 011005.
[51] www.flapw.de (accessed: July 2023).